Molecular Simulation of Carbon Dioxide Adsorption in Chemically and Structurally Heterogeneous Porous Carbons

C.M. Tenney and C.M. Lastoskie
Department of Civil and Environmental Engineering, University of Michigan, Ann Arbor, MI 48109-2125; cmlasto@umich.edu (for correspondence)

Published online 28 November 2006 in Wiley InterScience (www.interscience.wiley.com). DOI 10.1002/ep.10168

Capture of carbon dioxide from fossil fuel power plants via adsorption and sequestration of carbon dioxide in unmineable coal seams are achievable near-term methods of reducing atmospheric emissions of this greenhouse gas. To investigate the influence of surface heterogeneity upon predicted adsorption behavior in activated carbons and coal, isotherms were generated via grand canonical Monte Carlo simulation for CO_2 adsorption in slit-shaped pores with underlying graphitic structure and several variations of chemical heterogeneity (oxygen and hydrogen content), pore width, and surface functional group orientation. Adsorption generally increased with increasing surface oxygen content, although exceptions to this trend were observed on structurally heterogeneous surfaces with holes or furrows that yield strongly adsorbing preferred binding sites. Among the heterogeneous pore structures investigated, those with coal-like surfaces adsorbed carbon dioxide more strongly than planar, homogeneous graphitic slit pores of comparable width. Electrostatic adsorbate–adsorbent interactions significantly influenced adsorption onto model surfaces. © 2006 American Institute of Chemical Engineers Environ Prog, 25: 343–354, 2006

Keywords: carbon sequestration, Monte Carlo simulation, activated carbon, coal, isotherm, adsorption

INTRODUCTION

Emission of carbon dioxide into the atmosphere from fossil fuel combustion is recognized as a major contributor to global warming. Although a transition to other energy storage media such as hydrogen may ultimately slow accumulation of greenhouse gases in the atmosphere, there is a growing realization that for at least the next two or three decades, the persistence of the petroleum economy will ensure the continuing escalation of atmospheric carbon dioxide levels [1]. Hence, there is renewed urgency to develop feasible methods for capture and long-term sequestration of carbon dioxide in geologic or oceanic reservoirs. Approximately 30% of the gaseous CO_2 emitted to the atmosphere comes from fossil fuel power plants [2]. Being large-scale point sources, the flue gases from these power plants are attractive candidates for engineered capture and sequestration of CO_2.

Current or proposed methods of CO_2 capture from flue gas include absorption, adsorption, cryogenic distillation, and membrane separation. Because adsorption performs optimally at low CO_2 concentrations (<2%) [3], adsorption is typically used as a final polishing step in a hybrid CO_2 capture system [2]. Efficient capture of CO_2 using adsorption requires solid adsorbents with high CO_2 selectivity and capacity. Research is currently underway to identify and develop such sorbents, which include both naturally occurring materials such as coal and synthetic materials such as activated carbons, molecular sieves, and zeolites [2].

Relative to other sequestration alternatives, long-term storage of CO_2 in unmineable coal seams is particularly attractive because it can be linked to enhanced extraction of methane, an economically valuable and relatively low-carbon fossil fuel [4, 5]. The propensity for fossil fuel-based power plants to be located in geological basins featuring such coal deposits has been identified as a factor favoring this sequestration strategy [6]. Experiments and pilot studies using both pure CO_2 and flue gas have established that CO_2 readily displaces adsorbed methane from coal, significantly increasing coal bed methane yields compared to conventional methods [7–9].

Modeling and simulation play a critical role in understanding, characterizing, and developing adsorption systems. Complex porous materials such as activated carbons and coals have frequently been modeled as a collection of independent, noninterconnecting slit pores with smooth, homogeneous graphitic walls (e.g. Refs. 10–20). Pore size distributions calculated using this idealized structure from isotherms for a particular probe gas at a particular temperature (e.g. nitrogen at 77 K) do not always accurately predict adsorption at other temperatures or for other adsorbates [21], and prediction of adsorption of gas mixtures can be particularly challenging [13, 14, 22, 23]. For this reason, more complex models have been developed in an attempt to account for the structural and/or chemical heterogeneity of these materials [24–31].

In this paper, the results of a molecular simulation study of carbon dioxide adsorption are reported for CO_2 uptake on several model carbon pore geometries featuring various extents of chemical and structural heterogeneity. The models and simulation methodology are described herein, followed by a presentation of results, a summation of conclusions, and identification of future areas of research.

Table 1. Lennard–Jones and charge parameters for three-site CO_2 model.

Atom	Coordinate (nm)	σ (nm)	ε/k_B (K)	Charge, q (e)
C	0	0.280	27.0	0.70
O	±0.116	0.305	79.0	−0.35

METHODOLOGY

Isotherms for CO_2 adsorption into laterally infinite slit-shaped pores were generated via grand canonical Monte Carlo (GCMC) simulation using periodic boundary conditions. All simulations were performed at a temperature of 273 K, slightly below the CO_2 critical temperature of 304 K. Details of GCMC simulation algorithms are well documented elsewhere (e.g. Refs. 32–34). The three-site TraPPE CO_2 model, which was optimized to reproduce pure component bulk vapor–liquid equilibria, was used in this study [35].

Table 1 lists the parameters used for this model. Each atomic site is characterized as a Lennard–Jones (LJ) sphere with a partial charge. The potential energy between two LJ sites on different molecules was calculated using the LJ 12-6 potential and the standard Lorentz-Berthelot mixing rules:

$$U_{\mathrm{LJ,ab}} = 4\varepsilon_{\mathrm{ab}}[(\sigma_{\mathrm{ab}}/r)^{12} - (\sigma_{\mathrm{ab}}/r)^{6}] \quad (1)$$

$$\sigma_{\mathrm{ab}} = (\sigma_{\mathrm{a}} + \sigma_{\mathrm{b}})/2 \quad (2)$$

$$\varepsilon_{\mathrm{ab}} = (\varepsilon_{\mathrm{a}}\varepsilon_{\mathrm{b}})^{1/2} \quad (3)$$

where σ_a and ϵ_a are the site diameter and potential well depth for site a, respectively, and r is the distance between sites a and b. The potential energy between two charged sites on different atoms is

$$U_{\mathrm{ch,ab}} = q_{\mathrm{a}}q_{\mathrm{b}}/(4\pi\varepsilon_0 r) \quad (4)$$

where q_a is the charge at site a and r is the distance between sites a and b. LJ and electrostatic fluid–fluid interactions were truncated at 2 nm.

The absorbent surfaces were varied to investigate the influence of chemical and topological heterogeneity upon CO_2 adsorption. Isotherms for the 10-4-3 graphite surface [36] were generated for comparison.

Table 2. Names and construction parameters for model surfaces constructed by cleaving a graphite crystal and appending H, OH, or COOH functional groups to the exposed edges of graphene layers.

Model surface name	Cleavage plane	Functional group	Attachment angle (°)	Attachment pattern
c0_H	$(\bar{1}010)$	H only	—	—
c2_H	$(\bar{1}012)$	H only	—	—
c0_OH_a0_6 × 8	$(\bar{1}010)$	OH	0	6 × 8
c0_OH_a90_6 × 8	$(\bar{1}010)$	OH	90	6 × 8
c0_COOH_a0_6 × 8	$(\bar{1}010)$	COOH	0	6 × 8
c0_COOH_a90_6 × 8	$(\bar{1}010)$	COOH	90	6 × 8
c2_COOH_a0_6 × 8	$(\bar{1}012)$	COOH	0	6 × 8
c0_COOH_a0_6 × 4	$(\bar{1}010)$	COOH	0	6 × 4
c0_COOH_a90_6 × 4	$(\bar{1}010)$	COOH	90	6 × 4
c2_COOH_a0_6 × 4	$(\bar{1}012)$	COOH	0	6 × 4

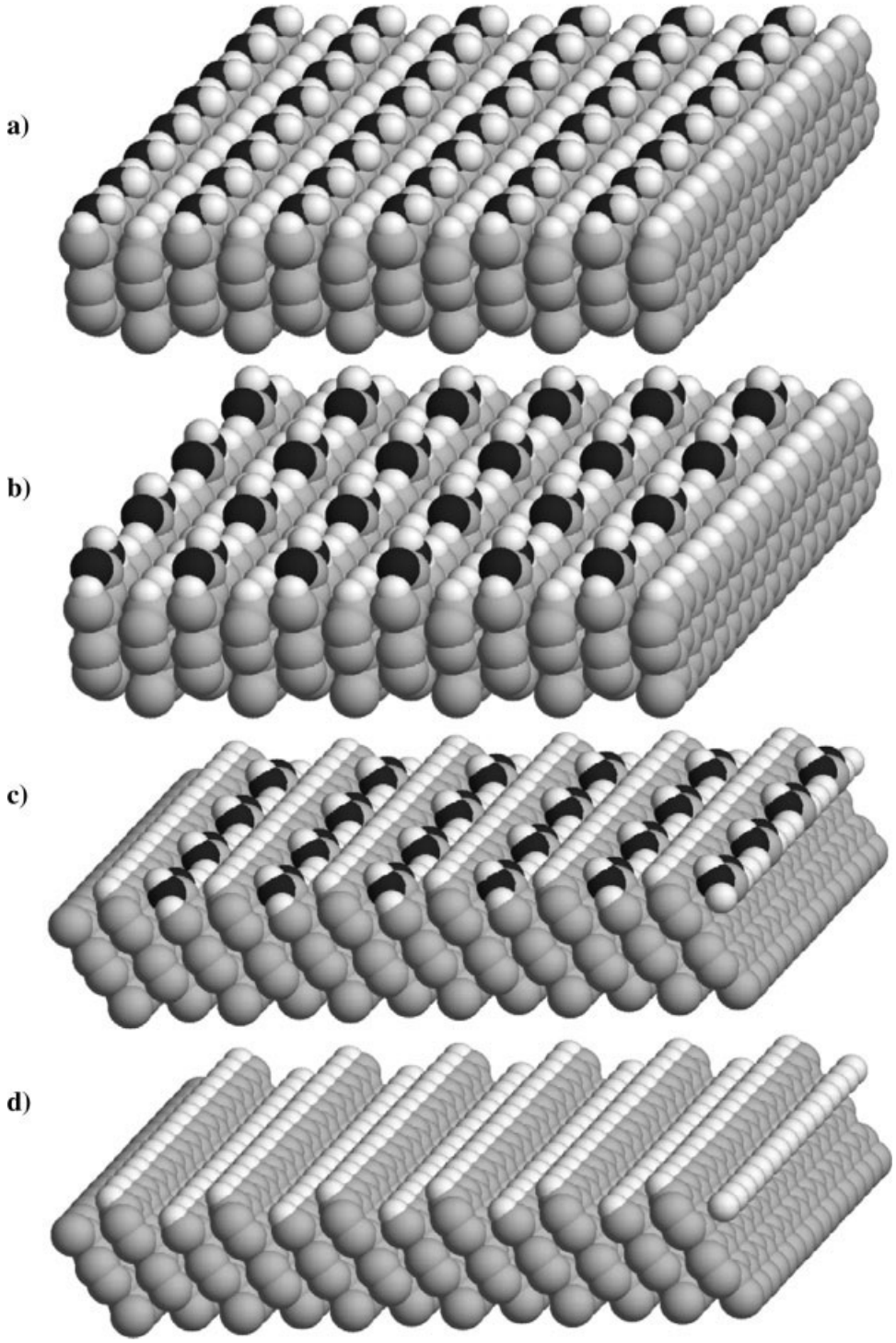

Figure 1. Examples of model surfaces summarized in Table 2: (a) c0_OH_a90_6 × 8, (b) c0_COOH_a0_6 × 4, (c) c2_COOH_a0_6 × 4, (d) c2_H. Surfaces are composed of carbon (light gray), oxygen (dark gray), and hydrogen (white) atoms.

The potential energy between a LJ site on an adsorbate molecule and a smooth, homogeneous 10-4-3 graphitic surface is

$$U_{sf} = 2\pi\varepsilon_{sf}\rho_s{\sigma_{sf}}^2\Delta[0.4(\sigma_{sf}/z)^{10} - (\sigma_{sf}/z)^4 - {\sigma_{sf}}^4/(3\Delta(z+0.61\Delta)^3)] \quad (5)$$

where ϵ_{sf} and σ_{sf} are calculated using the Lorentz-Berthelot mixing rules, Δ is the distance between graphene layers, and ρ_s is the solid density. The potential parameters used for graphite were: $\sigma_C = 0.34$ nm, $\epsilon_C/k_B = 28.0$ K, $\Delta = 0.335$ nm, and $\rho_s = 114$ nm^{-3} [36].

One set of model surfaces used in this study were generated by (1) cleaving a graphite crystal parallel to

Table 3. Lennard–Jones and charge parameters used to represent atoms in model surfaces.

Surface	Atom or site	σ (nm)	ε/k_B (K)	Charge, q (e)
graphite	C (aromatic)	0.340	28.0	—
cleaved graphite, H appended	C (aromatic)	0.340	28.0	−0.16
	H	0.240	12.0	0.16
cleaved graphite, OH appended	C (aromatic)	0.340	28.0	0.30
	O	0.310	79.0	−0.60
	H	0.130	30.0	0.30
cleaved graphite, COOH appended	C (aromatic)	0.340	28.0	−0.06
	C (COOH)	0.340	28.0	0.75
	O (=O)	0.310	79.0	−0.50
	O (—O—H)	0.310	79.0	−0.55
	H	0.130	30.0	0.36
coal-like surface, explicit H	C	0.340	28.0	varies
	O	0.310	79.0	varies
	H	0.130	30.0	varies
coal-like surface, implicit H	C (aromatic)	0.360	66.0	—
	CH (aromatic)	0.356	94.6	—
	CH_2	0.385	85.6	—
	C (other)	0.340	66.0	—
	O (all)	0.310	125.0	—

the $(\bar{1}010)$ or $(\bar{1}012)$ planes (perpendicular or slanted relative to the basal plane of graphite, respectively) and (2) attaching H, OH, or COOH functional groups in varying concentrations onto the exposed graphite carbon atoms so as to maintain sp^2 hybridization. In this manner, the effect of surface chemical heterogeneity (as manifested by the presence of oxygen-containing surface functional groups) was investigated for CO_2 adsorption in carbon micropores while still maintaining the periodicity and low dimensionality associated with the graphite slit pore geometry. All model surfaces were assumed to be rigid. The number of pendant OH or COOH groups and their angle of attachment to the surface were varied. Table 2 lists the surfaces examined in this study and provides, with the cleavage plane of the underlying carbon structure, the type and density of the appended functional group, and the attachment angle for the surface groups identified for each model surface. Where applicable, the surfaces on opposing walls of a slit pore were reversed relative to one other (i.e. not simply reflected across the center plane of the pore).

Figure 1 shows four of these model surfaces to a depth of ∼0.5 nm below the cleavage plane. For the GCMC simulations, each model structure extended ∼2.2 nm below the cleavage plane. The simulation cells spanned ∼4.0–4.8 nm in the lateral directions and were sized to accommodate 12 graphene edge planes with 16 exposed carbon atoms per edge. This resulted in 4032 and 4992 aromatic carbon atoms per simulation cell for the $(\bar{1}010)$ and $(\bar{1}012)$ surfaces, respectively. The highest density arrangements of OH or COOH functional groups occupied alternating exposed carbon sites on alternating graphene layers, resulting in a maximum of $6 \times 8 = 48$ oxygen-bearing functional groups per simulation cell. Sites not occupied by OH or COOH groups were saturated with H atoms. Note that the resulting C:O ratio for these model surfaces is not in itself particularly significant because the thickness of the underlying graphitic structure was arbitrarily chosen.

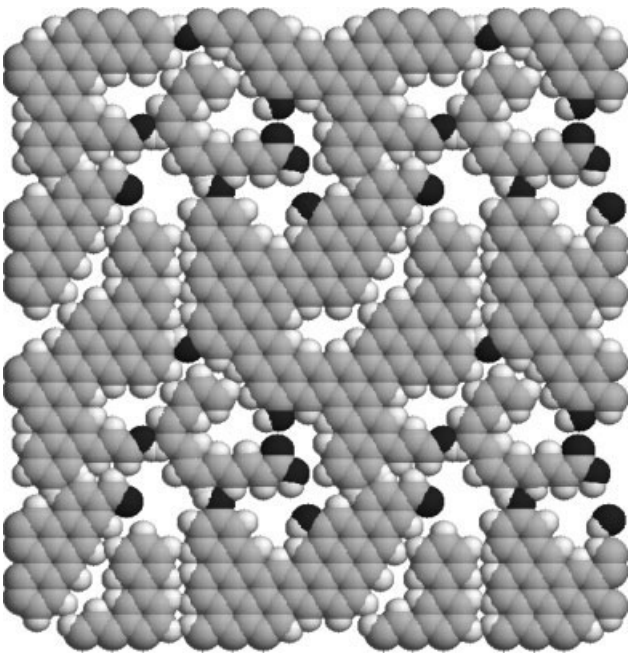

Figure 2. Top view of the coal-like model surface composed of carbon (light gray), oxygen (dark gray), and hydrogen (white) atoms.

The short-ranged nature of the dispersion and dipole–quadrupole adsorbate–adsorbent interactions in this study suggests that the carbon atoms more than ∼0.5 nm below the cleavage plane do not exert a major influence on CO_2 adsorption. The solid–fluid interaction energy includes both LJ and electrostatic contributions. Every atom in the surface structure was

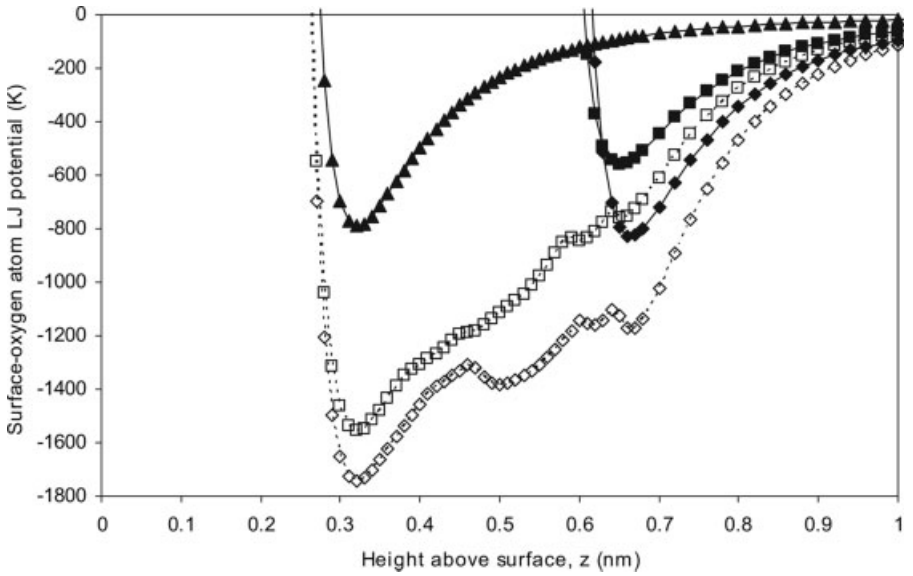

Figure 3. Mean (filled symbols) and minimum (open symbols) adsorbate–adsorbent Lennard–Jones (LJ) potentials for a CO_2 oxygen site versus distance above the surface for coal-like model surfaces with explicit hydrogen atoms (squares) and implicit hydrogen atoms (diamonds). The one-dimensional potential for the Steele surface (triangles) is shown for comparison.

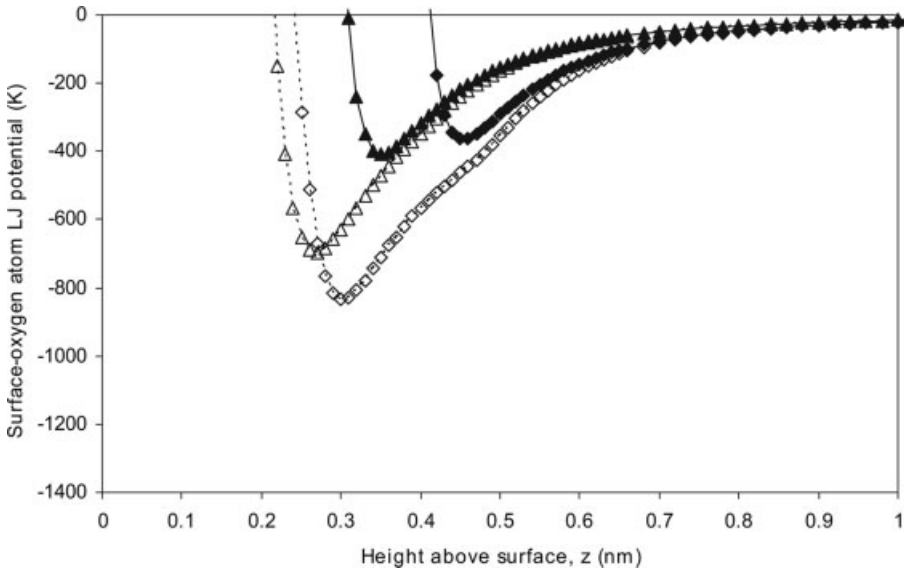

Figure 4. Mean (filled symbols) and minimum (open symbols) surface-fluid potential for a Lennard–Jones (LJ) CO_2 oxygen site versus distance above the surface for the c0_H (triangles) and c2_H (diamonds) model surfaces.

represented as a LJ site, and partial charges were assigned to each atom in the appended functional groups and to the carbon atom to which the groups are attached to the graphite surface. Table 3 lists the dispersion and charge parameters used to describe the atoms in these surfaces. Given the idealized nature of these surfaces, the force fields were not tuned to reproduce results from experimental adsorption measurements. The selected LJ parameter values are comparable to values used elsewhere [25, 37]. The assigned partial charges were based upon results obtained from *ab initio* calculations for representative ~100 atom polycyclic aromatic hydrocarbons performed using the Hartree-Fock method, 6-31g(d,p) basis set, and Mulliken charge analysis with the Gaussian 03 software package.

Another model heterogeneous surface used in the molecular simulations is shown in Figure 2. This surface has a carbon content similar to that of a typical coal [38, 39], and was oriented parallel to the basal plane of the underlying graphite. To create a surface with both chemical and topological heterogeneity, selected carbon atoms from the top graphene layer were either removed entirely or replaced with oxy-

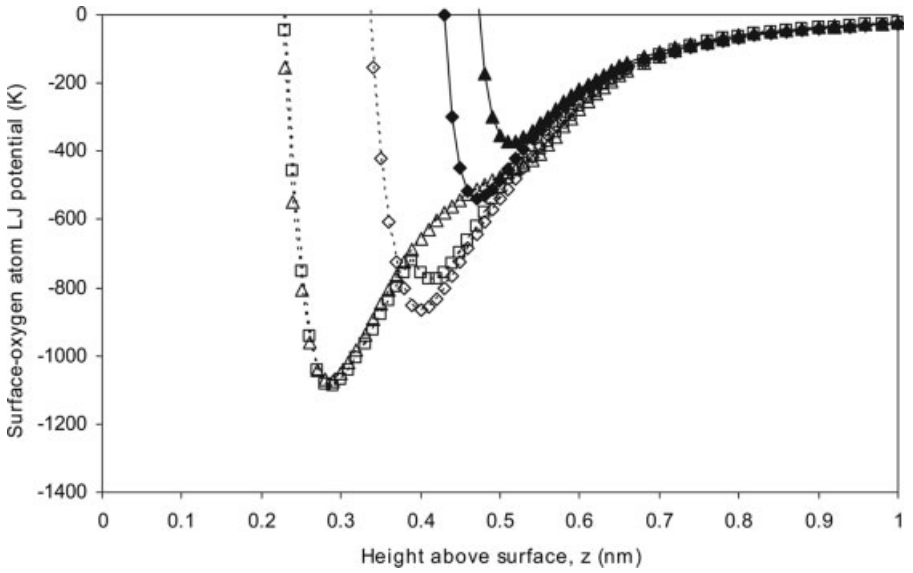

Figure 5. Mean (filled symbols) and minimum (open symbols) Lennard–Jones (LJ) potential for an oxygen CO_2 site versus distance above surface for the c0_COOH_a0_6 × 8 (triangles), c2_COOH_a0_6 × 8 (diamonds), and c0_COOH_a90_6 × 8 (squares) surfaces. The average potential for the c0_COOH_a90_6 × 8 surface coincides with that for the c0_COOH_a0_6 × 8 surface and is omitted for clarity.

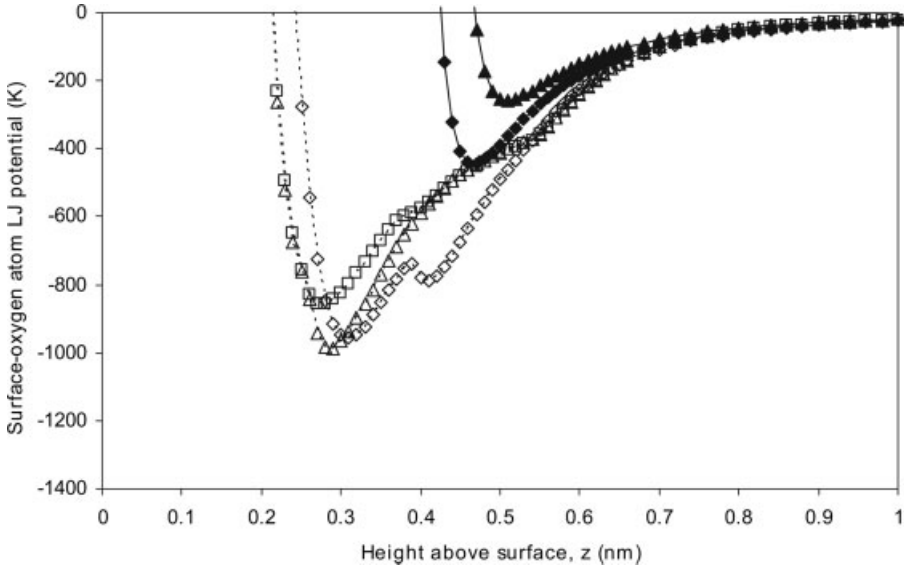

Figure 6. Same notation as in Figure 5, except for the 6 × 4 rather than the 6 × 8 surfaces.

gen- and hydrogen-containing functional groups, yielding a 212-atom surface structurally similar to that used by Vishnyakov *et al.* [25]. Simulations for the resulting surface were performed using three models of varying complexity and computational expense. First, the most complex and computationally intensive model represented each carbon, oxygen, and hydrogen atom in the top layer of the surface with both a LJ sphere and a point charge. To allow direct comparison with results from other model surfaces in this study, the LJ parameters chosen for this model were unchanged from those described above (see Table 3). Point charges for each surface atom (not listed) were obtained from *ab initio* calculations using the Hartree-Fock method, 6-31g basis set, and Mulliken charge analysis with the Gaussian 03 software package.

To study the importance of adsorbate–adsorbent electrostatic interactions, a second model used the same LJ parameters as the first but omitted all surface point charges. The third and least computationally expensive model omitted surface point charges and used a set of LJ parameters derived from Vishnyakov *et al.* [25] which only implicitly account for the presence of hydrogen atoms (see Table 3). For each of these three models, the adsorbate–adsorbent interac-

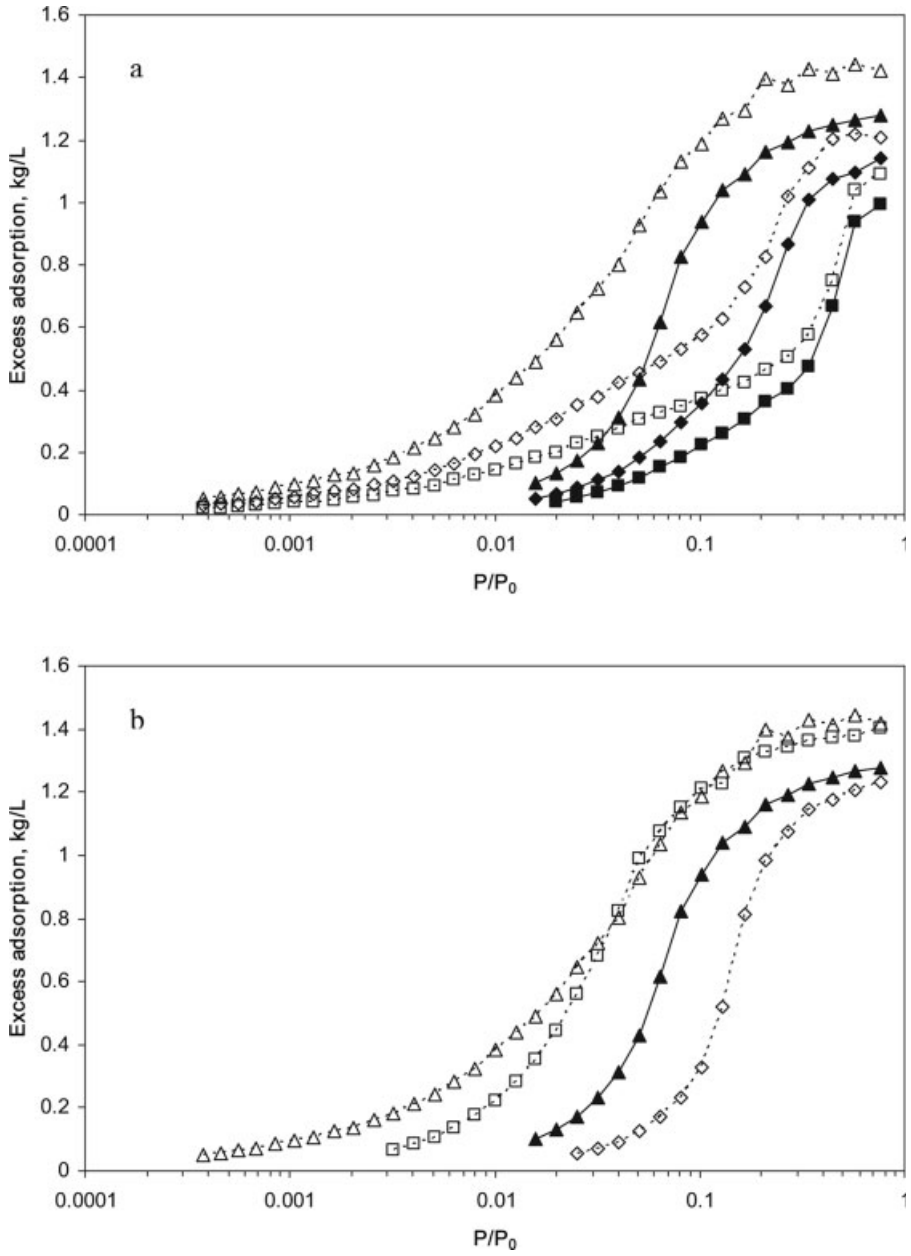

Figure 7. (a) Excess CO_2 adsorption isotherms at 273 K for 2.4 (squares), 1.8 (diamonds), and 1.35 (triangles) nm slit pores with Steele graphite surfaces (solid symbols) or coal-like surfaces with explicit hydrogen atoms and charges (open symbols). (b) Excess CO_2 adsorption isotherms at 273 K for 1.35 nm slit pores with Steele graphite surfaces (solid triangles), coal-like surfaces with explicit hydrogen atoms and charges (open triangles), coal-like surfaces with explicit hydrogen atoms but without charges (open diamonds), and coal-like surfaces with implicit hydrogen atoms (open squares).

tions for the subsurface layers in this structure were modeled using the 10-4-3 potential.

Simulations were performed for nominal pore widths $H = 1.35$, 1.8, and 2.4 nm, where for a graphitic slit pore, H is measured from the centers of the carbon atoms on the surface layers of the opposing pore walls. Pore widths of this size range are characteristic of the pore size distributions obtained for typical coal samples [8]. The pore widths of the heterogeneous model surfaces considered in this study were adjusted slightly so that the total available pore volume matched with that of a homogeneous graphitic slit pore of comparable surface area and similar nominal pore width. Available pore volume is defined here as the region of the pore volume where the LJ portion of the adsorbate–adsorbent potential has a zero or negative value.

To reduce the computational burden required for the molecular simulations, separate three-dimensional solid–fluid potential maps were generated for the dispersion and electrostatic interactions between the adsorbate atoms and the adsorbent surface by summing

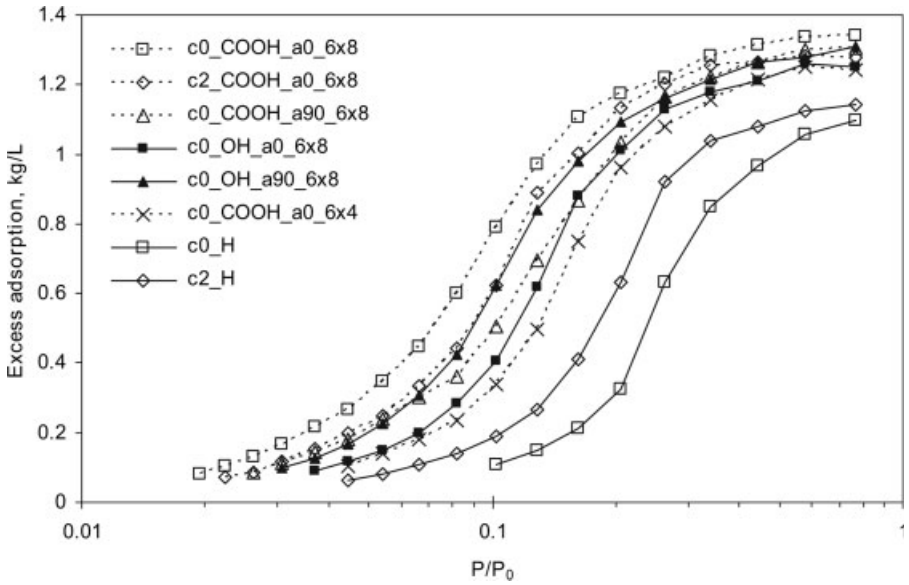

Figure 8. Excess CO_2 adsorption isotherms for 1.35 nm slit pores for various model surfaces at 273 K.

over all of the explicitly represented surface atoms prior to GCMC simulation. These summations were truncated at ~6 nm for LJ interactions and at ~60 nm for electrostatic interactions. The maps were discretized onto a 0.01 nm grid. The potential energy between the adsorbent and a particular CO_2 LJ site or charge site was calculated via linear interpolation between grid points. Convergence of the simulation results using truncation and discretization was verified (results not shown). Excess adsorption versus P/P_0 was calculated from absolute adsorption versus fugacity simulation results using thermodynamic equation of state data for carbon dioxide from the NIST Chemistry WebBook [40].

RESULTS AND DISCUSSION

Figures 3–6 show the mean and minimum adsorbate–adsorbent LJ potentials for an oxygen site on the CO_2 molecule as a function of the site distance above the carbon surface for various model surfaces. For the Steele 10-4-3 surface and the coal-like surface, the $z = 0$ plane passes through the centers of the carbon atoms in the top graphene layer. For the other surfaces, the $z = 0$ plane passes through the centers of the aromatic carbon atoms to which the OH or COOH functional groups were attached. The total CO_2-adsorbent potential is the sum of the potential interactions for the three constituent LJ sites (two oxygen and one carbon), plus the electrostatic interactions, if applicable. The latter are a function of both distance and orientation relative to the surface.

Figure 7a presents excess adsorption isotherms for slit pores with Steele graphite surfaces and coal-like surfaces with explicit hydrogen atoms and point charges at three different pore widths. Figure 7b repeats the 1.35 nm slit pore results from Figure 7a and shows for comparison results from simulations using the uncharged explicit-H and implicit-H coal-like surface models. Figure 8 reports excess adsorption isotherms for 1.35 nm slit pores with various truncated graphite model surfaces substituted with H, OH, or COOH surface groups. Continuous filling rather than phase transitions were observed in the isotherms for the 1.35-nm slit pores of all surface compositions, and capillary condensation occurred only in the largest (2.4 nm) pore size considered. Adsorption/desorption hysteresis was not observed for any of the surfaces studied. Figure 9 shows snapshots from GCMC simulations at $P/P_0 = 0.001$, 0.1, and 0.44 for 2.4 nm slit pores with coal-like surfaces with explicit hydrogen atoms and surface charges. Figure 10 shows a snapshot at $P/P_0 = 0.1$ for one surface of a 2.4 nm slit pore with c0_COOH_a0_6 × 8 surfaces.

The deep trough at $z \sim 0.31$ nm in the minimum potential curves for the coal-like surfaces in Figure 3 is indicative of a hole or cavity in the first surface layer. The low energy at this site results from interactions with the underlying surface layer and surface atoms around the edge of the hole. The large difference between the minimum and mean potential curves for the coal-like surface is a consequence of the surface roughness. The broadness of the minimum potential curve for the coal-like surface, compared with the potential curve for the Steele surface, suggests that monolayer formation and wetting of the coal-like surface by CO_2 should occur over a wider range of pressures than for the Steele surface. This expectation is confirmed in the excess adsorption isotherms reported in Figure 7 for slit pores with Steele- and coal-like surfaces. Because the minimum potential for the coal-like surface is significantly lower than the Steele potential, it was expected that CO_2 adsorption would universally occur at lower pressures for the coal-like surface than for the Steele surface. This is not observed, however, in Figure 7b for the uncharged explicit-H surface model, for perhaps two reasons. First, it is possible that the

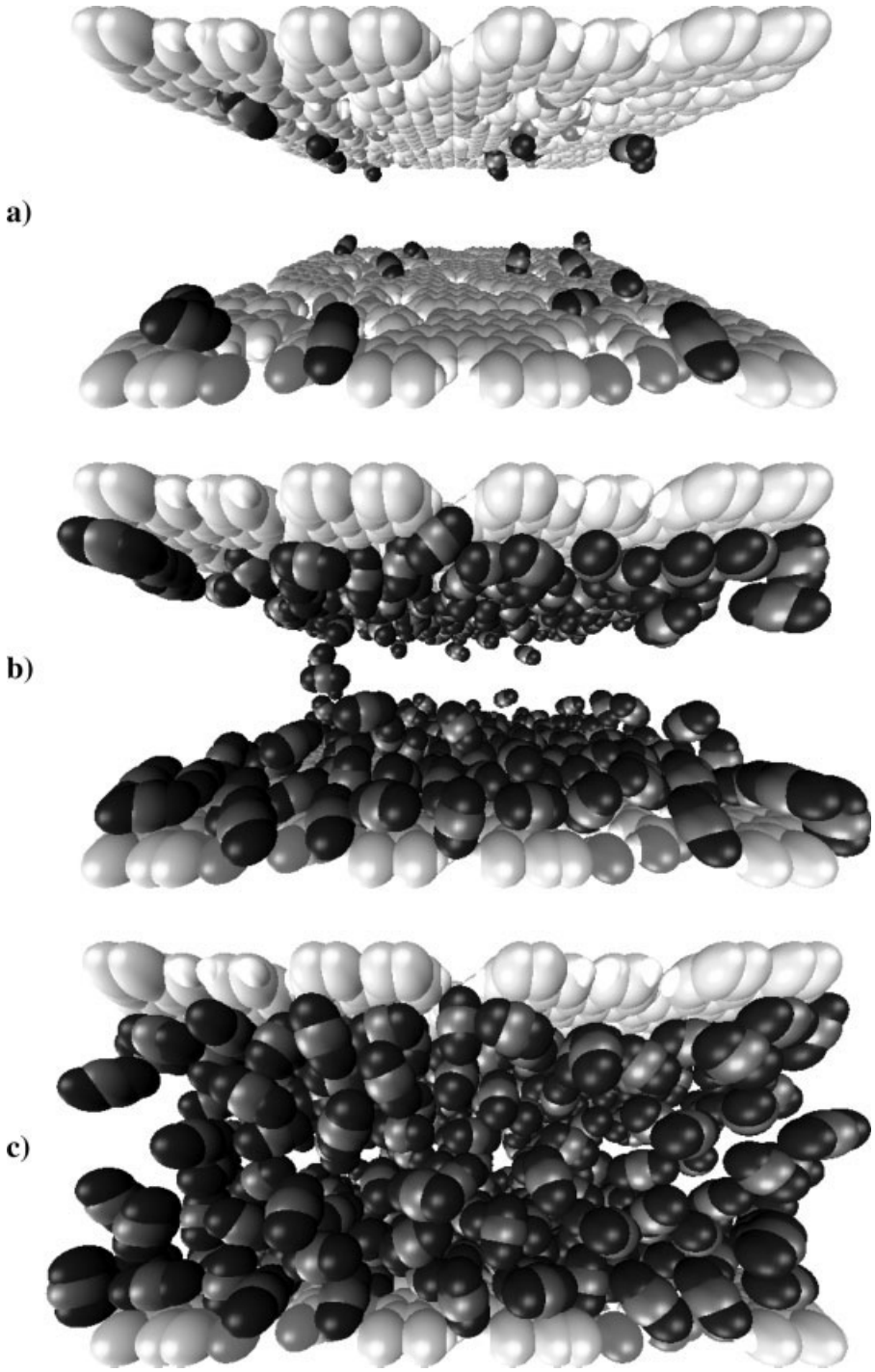

Figure 9. Snapshots of CO_2 adsorption at 273 K and $P/P_0 = 0.001$, 0.1, and 0.44 (a–c, respectively) in 2.4 nm slit pores having coal-like surfaces with explicit hydrogen atoms and charges.

low energy "cavity" sites on the coal-like surface are too few in number to compensate for the weaker mean potential interaction of CO_2 with the coal-like surface. Second, because CO_2 is a linear molecule, orientation and size exclusion play a significant role in its adsorption onto surface defect structures, and thus energetically favorable sites for the adsorption of a monatomic adsorbate (e.g. the oxygen site of CO_2) may not be accessible to the polyatomic CO_2 molecule. Adsorbate–adsorbate interactions, which increase as the surface coverage increases, also influence binding at particular surface sites.

For simulations of coal-like surfaces in which electrostatic interactions were included, electrostatic adsorbate–adsorbent interactions accounted for 60–70% of the total adsorbate–adsorbent potential energy at low surface coverage, which significantly increased adsorption of CO_2 relative to the uncharged case. In

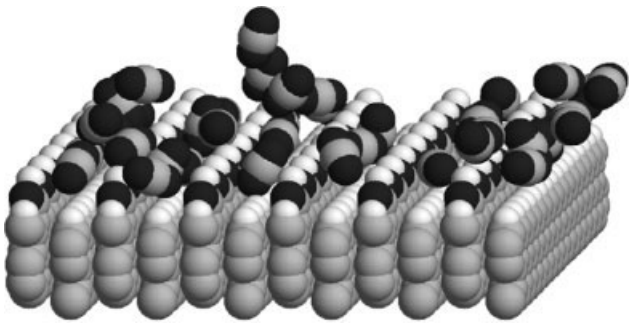

Figure 10. Snapshot of CO_2 adsorption on a c0_COOH_a0_6 × 8 surface in a 2.4 nm slit pore at 273 K and $P/P_0 = 0.1$.

contrast, for simulations with the idealized heterogeneous model surfaces, the electrostatic adsorbate–adsorbent interactions accounted for only 20–30% of the total adsorbate–adsorbent potential energy, and CO_2 adsorbed less strongly onto these surfaces than onto the Steele surface. While the relatively large LJ interaction potentials for the uncharged implicit-H coal-like surface resulted in high-pressure adsorption behavior similar to that for the charged explicit-H surface, low-pressure adsorption is still greatly reduced (Figure 7b).

A comparison of the LJ potentials of Figure 4 indicates that the c2_H model surface is topologically rougher and possesses sites that bind more strongly than the c0_H surface. As shown in Figure 8, for the c2_H surface, the isotherm is broader and more CO_2 adsorption occurs at lower relative pressures than for the c0_H surface.

Figure 5 compares the mean and minimum potentials for the three model surfaces with COOH functional groups arranged in a 6 × 8 pattern. The c0_COOH_a90_6 × 8 and c0_COOH_a0_6 × 8 surfaces differ only in the attachment angle of the COOH functional group, and it is seen that the mean potentials for these surfaces overlap. In contrast, the minimum potential for the c0_COOH_a90_6 × 8 surface has a secondary minimum at $z = 0.41$ nm that is not present in the minimum potential for the c0_COOH_a0_6 × 8 surface. Relative to the other surfaces, the c2_COOH_a0_6 × 8 surface is topologically smoother and energetically more uniform, with a higher minimum potential but a lower mean potential. As can be seen in Figure 8, CO_2 adsorption in the c0_COOH_a0_6 × 8 slit pore is significantly enhanced relative to the other two surfaces with the same arrangement of COOH sites. Although initial adsorption of CO_2 into the c2_COOH_a0_6 × 8 and c0_COOH_a90_6 × 8 slit pores occurs at the same relative pressure, pore filling is completed at a slightly lower pressure for the c2_COOH_a0_6 × 8 surface, consistent with the topological differences between the two surfaces.

The surfaces represented in Figure 6 have half the COOH functional group site density of the surfaces represented in Figure 5. In general, this results in a weaker LJ interaction potential (as indicated by Figure 6) and a decrease in CO_2 adsorption (as seen in the c0_COOH_a0_6 × 4 curve of Figure 8). The general ordering of the mean potentials for the various surfaces remains unchanged, with the exception of the c2_COOH_a0 surface, which acquires a secondary minimum in its potential for a 6 × 4 ordering of the functional groups that is absent in the 6 × 8 ordering; and the c0_COOH_a90 surface, which has a secondary minimum in the 6 × 8 ordering but not in the 6 × 4 ordering. These differences indicate that the orientation of surface functional groups can significantly influence the energy landscape, and hence the resulting GCMC isotherms. Figure 10 shows how CO_2 preferentially adsorbs in the energetically favorable valleys between the rows of COOH surface groups in the c0_COOH_a0_6 × 8 slit pore. This CO_2 alignment was observed for many of the model surfaces investigated in this study.

The mean and minimum adsorbate–adsorbent potentials for surfaces with OH functional groups (not pictured) featured single minima ~100 K higher in energy (ϵ/k_b) than those for corresponding surfaces with COOH sites. As seen in Figure 8, with the exception of the c0_COOH_a90_6 × 8 surface, surfaces with COOH functional groups generally adsorb CO_2 more strongly than surfaces with an equivalent number of OH groups. It was noted that the rank ordering of surfaces with OH functionality, but the same underlying cleavage plane structure, in terms of their adsorption strength was somewhat different than the rank ordering for the same surfaces with COOH functional groups. While there is significant variation among the isotherms for the various 6 × 8 surfaces, the corresponding set of isotherms (not shown) for CO_2 adsorption on the 6 × 4 surfaces were much more similar. The cleavage plane of the adsorbent surface was observed to have a significant effect on CO_2 adsorption, particularly so in the case of unsubstituted (H-only) surfaces for which substantial differences in the isotherms of the c0_H and c2_H surfaces were noted.

CONCLUSIONS

Isotherms were generated via GCMC simulations for adsorption of CO_2 into graphite-based model slit pores with surfaces of varying chemical and structural heterogeneity. The pressure at which pore filling with CO_2 occurred varied over approximately one order of magnitude for pores in the size range between 1.35 nm and 2.4 nm. Electrostatic adsorbate–adsorbent interactions significantly influenced adsorption onto coal-like model surfaces. Increasing the surface density of oxygen-containing functional groups generally increased CO_2 adsorption and lowered the pore filling pressure. However, exceptions were noted, and in some cases, outwardly small differences between surfaces resulted in very different isotherms. For the coal-like model pores with explicit charge interactions simulated in this study, low-pressure CO_2 uptake was significantly enhanced, and the excess adsorption at the saturation pressure was slightly

increased, relative to CO_2 adsorption in comparably sized graphite slit pores.

CO_2 capture and sequestration on natural or synthetic adsorbents occurs in a complex, mixed-species environment. Models and methods to better analyze and predict adsorption under these conditions continue to be developed. Anticipated future research will extend the coal-like model surface described herein to random, three-dimensional coal structures constrained by coal composition data and chemical bond distribution are also being developed. These model structures will be used to investigate CO_2 adsorption selectivity and capacity for mixed-gas systems relevant to CO_2 capture and sequestration.

LITERATURE CITED

1. Houghton, J.T., Ding, Y., Griggs, D.J., Noguer, M., van der Linden, P.J., Dai, X., Maskell, K., & C.A. Johnson (Eds.) (2001). Climate change 2001: The scientific basis. Contribution of working group 1 to the third assessment report of the intergovernmental panel on climate change (p. 881). Cambridge, United Kingdom:Cambridge University Press.
2. Aaron, D., & Tsouris, C. (2005). Separation of CO_2 from flue gas: A review, Separation Science and Technology, 40, 321–348.
3. Audus, H. (1997). Greenhouse gas mitigation technology: An overview of the CO_2 capture and sequestration studies and further activities of the IEA greenhouse gas R&D programme, Energy, 22, 217–221.
4. Gunter, W.D., Gentzis, T., Rottenfusser, B.A., & Richardson, R.J.H. (1997). Deep coalbed methane in Alberta, Canada: A fuel resource with the potential of zero greenhouse gas emissions, Energy Conversion and Management, 38 (Suppl. 1), S217–S222.
5. Pashin, J.C., & McIntyre, M.R. (2003). Temperature-pressure conditions in coalbed methane reservoirs of the Black Warrior basin: Implications for carbon sequestration and enhanced coalbed methane recovery, International Journal of Coal Geology, 54, 167–183.
6. Hitchon, B., Gunter, W.D., Gentzis, T., & Bailey, R.T. (1999). Sedimentary basins and greenhouse gases: A serendipitous association, Energy Conversion and Management, 40, 825–843.
7. Pashin, J.C., Groshong R.H., Jr., & Carroll, R.E. (2001). Carbon sequestration potential of coalbed methane reservoirs in the Black Warrior basin: A preliminary look, in 2001 International Coalbed Methane Symposium, Tuscaloosa, AL, May 14–18, 2001, pp. 51–62.
8. Tsotsis, T.T., Patel, H., Najafi, B.F., Racherla, D., Knackstedt, M.A., & Sahimi, M. (2004). Overview of laboratory and modeling studies of carbon dioxide sequestration in coal beds, Industrial & Engineering Chemistry Research, 43, 2887–2901.
9. White, C.M., Smith, D.H., Jones, K.L., Goodman, A.L., Jikich, S.A., LaCount, R.B., DuBose, S.B., Ozdemir, E., Morsi, B.I., & Schroeder, K.T. (2005). Sequestration of carbon dioxide in coal with enhanced coalbed methane recovery—A review, Energy & Fuels, 19, 659–724.
10. Lastoskie, C.M., Gubbins, K.E., & Quirke, N. (1993). Pore size distribution analysis of microporous carbons: A density functional theory approach, Journal of Physical Chemistry, 97, 4786–4796.
11. Lastoskie, C.M., Gubbins, K.E., & Quirke, N. (1993). Pore size heterogeneity and the carbon slit pore: A density functional theory model, Langmuir, 9, 2693–2702.
12. Lastoskie, C.M., Gubbins, K.E., & Quirke, N. (1997). Structure of porous sorbents: Analysis using density functional theory and molecular simulation, Studies in Surface Science & Catalysis, 104, 745–775.
13. Quirke, N., & Tennison, S.R.R. (1996). The interpretation of pore size distributions of microporous carbons, Carbon, 34, 1281–1286.
14. Heuchel, M., Davies, G.M., Buss, E., & Seaton, N.A. (1999). Adsorption of carbon dioxide and methane and their mixtures on an activated carbon: Simulation and experiment, Langmuir, 15, 8695–8705.
15. Lastoskie, C.M. (2000). A modified Horvath-Kawazoe method for micropore size analysis, Studies in Surface Science & Catalysis, 128, 475–484.
16. Ravikovitch, P.I., Vishnyakov, A., Russo, R., & Neimark, A.V. (2000). Unified approach to pore size characterization of microporous carbonaceous materials from N-2, Ar, and CO_2 adsorption isotherms, Langmuir, 16, 2311–2320.
17. Samios, S., Stubos, A.K., Papadopoulos, G.K., Kanellopoulos, N.K., & Rigas, F. (2000). The structure of adsorbed CO_2 in slitlike micropores at low and high temperature and the resulting micropore size distribution based on GCMC simulations, Journal of Colloid and Interface Science, 224, 272–290.
18. Dombrowski, R.J., Lastoskie, C.M., & Hyduke, D.R. (2001). The Horvath-Kawazoe method revisited, Colloids & Surfaces A: Physicochemical and Engineering Aspects, 187, 23–39.
19. Dombrowski, R.J., & Lastoskie, C.M. (2002). A two-stage Horvath-Kawazoe adsorption model, Studies in Surface Science & Catalysis, 144, 99–106.
20. Cao, D.P., & Wu, J.Z. (2005). Modeling the selectivity of activated carbons for efficient separation of hydrogen and carbon dioxide, Carbon, 43, 1364–1370.
21. Dombrowski, R.J., Hyduke, D.R., & Lastoskie C.M. (2000). Pore size analysis of activated carbons from argon and nitrogen porosimetry using density functional theory, Langmuir, 16, 5041–5050.
22. Davies, G.M., & Seaton N.A. (1999). Development and validation of pore structure models for adsorption in activated carbons, Langmuir, 15, 6263–6276.
23. Sweatman, M.B., & Quirke, N. (2001). Characterization of porous materials by gas adsorption: Comparison of nitrogen at 77 K and carbon

dioxide at 298 K for activated carbon, Langmuir, 17, 5011–5020.
24. Lastoskie, C.M., Gubbins, K.E., & Quirke, N. (1994). Pore size distribution analysis and networking studies of microporous sorbents, Studies in Surface Science & Catalysis, 87, 51–61.
25. Vishnyakov, A., Piotrovskaya, E.M., & Brodskaya, E.N. (1998). Capillary condensation and melting/freezing transitions for methane in slit coal pores, Adsorption—Journal of The International Adsorption Society, 4, 207–224.
26. Davies, G.M., & Seaton, N.A. (1998). The effect of the choice of pore model on the characterization of the internal structure of microporous carbons using pore size distributions, Carbon, 36, 1473–1490.
27. Lastoskie, C.M., & Gubbins, K.E. (2000). Characterization of porous materials using density functional theory and molecular simulation, Studies in Surface Science & Catalysis, 128, 41–50.
28. Lastoskie, C.M., & Gubbins, K.E. (2001). Characterization of porous materials using molecular theory and simulation, Advances in Chemical Engineering, 28, 203–250.
29. Schoen, M. (2002). Capillary condensation between mesoscopically rough surfaces, Colloids and Surfaces A: Physicochemical and Engineering Aspects, 206 (1–3, special issue), 253–266.
30. Pikunic, J., Lastoskie, C.M., & Gubbins, K.E. (2002). Molecular modeling of adsorption from the gas phase. In F. Schüth, K.S.W. Sing, & J. Weitkamp (Eds.), Handbook of porous solids (pp. 182–236), Weinheim, Germany: Wiley-VCH.
31. Pikunic, J., Clinard, C., Cohaut, N., Gubbins, K.E., Guet, J.M., Pellenq, R.J.M., Rannou, I., & Rouzaud, J.N. (2003). Structural modeling of porous carbons: Constrained reverse Monte Carlo method, Langmuir, 19, 8565–8582.
32. Nicholson, D., & Parsonage, N.G. (1982). Computer simulation and the statistical mechanics of adsorption, London, UK: Academic Press.
33. Allen, M.P., & Tildesley, D.J. (1987). Computer simulation of liquids, Oxford, UK: Oxford Science.
34. Frenkel, D., & Smit, B. (1996). Understanding molecular simulation, San Diego, CA: Academic Press.
35. Potoff, J.J., & Siepmann, J.I. (2001). Vapor–liquid equilibria of mixtures containing alkanes, carbon dioxide, and nitrogen, AIChE Journal, 47, 1676–1682.
36. Steele, W.A. (1974). The interaction of gases with solid surfaces, New York: Pergamon.
37. Freindorf, M., & Gao, J.L. (1996). Optimization of the Lennard–Jones parameters for a combined ab initio quantum mechanical and molecular mechanical potential using the 3-21G basis set, Journal of Computational Chemistry, 17, 386–395.
38. Fitzgerald, J.E., Sudibandriyo, M., Pan, Z., Robinson, R.L., & Gasem, K.A.M. (2003). Modeling the adsorption of pure gases on coals with the SLD model, Carbon, 41, 2203–2216.
39. Ozdemir, E., Morsi, B.I., & Schroeder, K. (2003). Importance of volume effects to adsorption isotherms of carbon dioxide on coals, Langmuir, 19, 9764–9773.
40. Lemmon, E.W., McLinden, M.O., & Friend, D.G. (2005). Thermophysical properties of fluid systems. In P.J. Linstrom, & W.G. Mallard (Eds.), NIST chemistry webbook, Gaithersburg, MD: National Institute of Standards and Technology. NIST standard reference database number 69, Available at **http://webbook.nist.gov**